Metastable B-doped FeNi compounds for permanent magnets without rare earths

Masahiro Sakurai [1,*] and James R. Chelikowsky [1,2,3]
[1] *Center for Computational Materials, Oden Institute for Computational Engineering and Sciences, The University of Texas at Austin, Austin, Texas 78712, USA*
[2] *McKetta Department of Chemical Engineering, The University of Texas at Austin, Austin, Texas 78712, USA*
[3] *Department of Physics, The University of Texas at Austin, Austin, Texas 78712, USA*

(Received 16 October 2019; revised 21 April 2020; accepted 14 July 2020; published 4 August 2020)

We apply first-principles calculations to metastable B-doped Fe-Ni compounds to compute their magnetic properties. We focus on crystal structures with tetragonal and orthorhombic lattices. Boron atoms, doped at interstitial sites, help in stabilizing noncubic Fe-Ni structures. At the same time, the dopants improve the magnetic properties, such as magnetocrystalline anisotropy, compared to FeNi alloys in the tetragonal $L1_0$-ordered structures. The calculated magnetocrystalline anisotropy constants of 1–2 $\mathrm{MJ/m^3}$ along with sufficient magnetic polarization saturation ($\geqslant$1 T) show the potential of our metastable Fe-Ni-B compounds for replacing rare-earth-based magnets in permanent-magnet applications.

DOI: 10.1103/PhysRevMaterials.4.084402

I. INTRODUCTION

Magnets play a crucial role in modern technologies. In particular, permanent magnets are indispensable components for magnet-based devices, such as electrical motors, hybrid vehicles, and data storage. The performance of a permanent magnet relies on its intrinsic magnetic properties, such as magnetic polarization saturation, magnetocrystalline anisotropy, and the Curie temperature [1–3]. Among the 3*d* transition-metal elements, iron provides high magnetic polarization saturation. Bulk iron, however, exhibits a negligible amount of magnetocrystalline anisotropy energy due to the cubic symmetry of its crystal lattice. For permanent magnet applications, iron is commonly alloyed with rare-earth elements, such as samarium (Sm), neodymium (Nd), and dysprosium (Dy). These rare-earth elements can enhance magnetocrystalline anisotropy significantly [4–6], leading to strong coercivity and a large maximum energy-product [$(BH)_{\max}$]. The demand for rare-earth elements continues to grow in recent years, giving rise to concerns about physical, environmental, and economical limitations on the supply of rare-earth elements [7].

Several efforts have been made to discover alternative magnetic materials that consist of earth-abundant, inexpensive elements [8,9]. Candidate materials proposed so far are mostly Fe-based or Co-based alloys. For example, the binary alloy with a face-centered tetragonal ("$L1_0$-ordered") structure [10], also know as tetrataenite has a good potential to exhibit moderate magnetic anisotropy [11–13]. The enhancement of magnetic anisotropy can be attributed to tetragonal distortion as in the case of tetragonal FeCo alloys [14]. New rare-earth-free magnets from recent experimental efforts also include Fe-rich ternary alloys, such as $Fe_{3+x}Co_{3-x}Ti_2$ ($0 \leqslant x \leqslant 3$) and $Fe_3Co_3Nb_2$ compounds [15,16]. The magnitude of magnetic anisotropy in these materials still fails to yield a high coercivity sufficient for permanent-magnet applications.

Addition of a third element into such binary systems can be an effective strategy to optimize their magnetic properties. In fact, popular rare-earth-based magnets, such as $Nd_2Fe_{14}B$ and $Sm_2Fe_{17}N_3$ compounds, contain a third element as a dopant [4,5]. Such dopants play a key role in stabilizing the atomic structures as well as improving the magnetic properties of rare-earth-based compounds [17].

Recent advances in synthetic methods make it possible to produce not only the lowest-energy phase but also metastable structures. For example, several metastable phases of Co_3N are synthesized using nonequilibrium synthetic methods [18]. The concurrent theoretical research clarifies that a Co_3N phase with a hexagonal $P6_3/mmc$ structure has better magnetic properties than the pure Co phase [19]. The nonequilibrium synthetic methods also lead to the development of magnetic alloys with interesting noncollinear spin textures [20,21].

A widely used approach to calculate the structural, electronic, and magnetic properties of materials from first principles is a combination of density-functional theory (DFT) [22,23] and pseudopotential theory [24]. A plane-wave method is a standard technique to the pseudopotential DFT. It has been applied to a wide range of nanoscale systems including magnetic materials [25]. We also employ a real-space method as an efficient implementation of the pseudopotential DFT [26–28], allowing us to generate accurate descriptions for various magnetic materials [29–33].

We carry out first-principles calculations to discover new rare-earth-free compounds that have high magnetocrystalline anisotropy and large magnetic polarization saturation. Here, we focus on B-doped Fe-Ni compounds with tetragonal and orthorhombic crystal lattices. We show that several Fe-Ni-B phases, identified as metastable structures, can exhibit high magnetocrystalline anisotropy and sufficient magnetization to be useful for permanent-magnet applications.

*masahiro@ices.utexas.edu

II. COMPUTATIONAL METHODS

Our first-principles calculations are based on the density-functional theory in a relativistic formalism [22,23,34,35]. We employ the generalized gradient approximation (GGA) for the exchange-correlation functional [36]. The spin-orbit interaction, a major cause of the magnetocrystalline anisotropy, is incorporated through relativistic pseudopotentials [37–40]. GGA calculations are done by using a plane-wave formalism with the QUANTUM ESPRESSO code [41,42] as well as a real-space formalism with the PARSEC code [26–28]. Real-space pseudopotentials are constructed with a partial core correction [43]. The wave functions are expanded in a plane-wave basis set with a kinetic energy cutoff of 65 Ry for plane-wave calculations, whereas a uniform real-space grid with a grid spacing of 0.3 a.u. (approximately 0.16 Å) is used for real-space calculations. We adopt the Monkhorst-Pack scheme [44] to carry out Brillouin-zone integrations with a momentum-space resolution of $2\pi \times 0.01$ a.u.$^{-1}$. This resolution is equivalent to a fine k-point grid of $16 \times 16 \times 16$ for tetragonal $L1_0$-ordered FeNi. Such a fine k-point sampling is necessary for achieving better convergence for the magnetic properties, especially for the magnetic anisotropy constant [40]. Structural relaxations are performed until a residual force is less than 0.001 Ry/a.u. In PARSEC, the relativistic Kohn-Sham equation is solved with subspace filtering algorithms based on Chebyshev polynomials [45–47]. Our filtering technique avoids computationally heavy full diagonalizations and can reduce computational time by more than an order of magnitude in comparison to conventional diagonalization-based methods.

III. MAGNETOCRYSTALLINE ANISOTROPY

Magnetic materials can exhibit energetically favorable ("easy") and unfavorable ("hard") directions for the orientation of the magnetic moments ($\vec{m}$), leading to an energy difference between the two states. Suppose the crystallographic c axis is the easy axis, the magnetic anisotropy energy, E_a, can be given by the total-energy difference between the two states where the magnetic moments are oriented along the easy and hard axes:

$$E_a = E(\vec{m} \perp \vec{c}) - E(\vec{m} \parallel \vec{c}). \tag{1}$$

The magnetic anisotropy energy can also be expressed as a power series with the angle, θ, between the easy axis and the magnetic moments. For a tetragonal crystal system, it reads

$$E_a(\theta) = K_1 V \sin^2\theta + K_2 V \sin^4\theta + \cdots, \tag{2}$$

where V is the volume of a system. The coefficients K_i ($i = 1, 2, \ldots$) are called the magnetocrystalline anisotropy constants. The second-order constant, K_1, is a dominant factor and higher-order constants can be neglected for most magnetic materials. In this approximation, the second-order constant, K_1, is calculated as $K_1 = E_a/V$.

We perform pseudopotential DFT calculations to compute the total energies of an Fe-Ni-B compound with two magnetic configurations, $E(\vec{m} \perp \vec{c})$ and $E(\vec{m} \parallel \vec{c})$. We then evaluate the magnetic anisotropy energy, E_a, and the second-order constant, K_1. The magnetic anisotropy energies of our metastable Fe-Ni-B compounds are found to be of the order of 1 meV per formula unit. We confirm that results from the plane-wave and real-space methods are consistent with each other. Typically, the difference in the magnetocrystalline anisotropy constant, K_1, is about 0.2 MJ/m^3. Trends in K_1 across the Fe-Ni-B system agree as well.

IV. RESULTS

A. Possible crystal structures

We introduce five space groups to be examined as possible symmetry groups for B-doped Fe-Ni compounds with a tetragonal or orthorhombic unit cell. (i) Space group $P4/mmm$ (space group No. 123) is one of the space groups in the tetragonal crystal system. The $P4/mmm$ symmetry can be found in various magnetic alloys, such as FeNi and FePt, forming a large family of $L1_0$-ordered binary magnets. (ii) Crystal structure with space group $I4/mmm$ (No. 139) is realized in several intermetallic compounds including Mn_2Ga. The tetragonal $D0_{22}$ phase of Mn_2Ga exhibits moderate magnetic anisotropy ($\sim$2 MJ/m^3) without relying on a rare-earth element [48]. (iii) Crystal structure with space group $I4/m$ (No. 87) is predicted as a lowest-energy structure of Co_5N with a tetragonal unit cell [49]. We expect Fe-Ni-B compounds to take an $I4/m$ structure as well by the similarity in the constituent elements. (iv) Orthorhombic crystal structure belonging to space group $Amm2$ (No. 38) is identified as one of the Fe-Co-N compounds that can exhibit a large magnetic anisotropy energy [49,50]. (v) Orthorhombic structure with space group $Cmcm$ (No. 63) is also discovered during the crystal-structure searches for Fe-Co-N alloys. The latter two space groups ($Amm2$ and $Cmcm$) are the most likely candidates for orthorhombic Fe-Ni-B structures.

Figure 1(a) shows the crystal structure of $L1_0$-ordered $P4/mmm$ FeNi phase. Fe atoms are on the basal and top planes of a face-centered tetragonal-like unit cell, whereas Ni atoms are at the face of four sides, forming layers of Fe and Ni alternated along the crystallographic c axis. We adopt this "layer-by-layer" arrangement as a structural motif to construct a candidate Fe-Ni-B structure. We explore possible atomic positions for Fe, Ni, and B atoms so that the resultant Fe-Ni-B compound can belong to one of the above-mentioned five space groups. Atomic positions and lattice constants are then optimized by DFT-GGA calculations. In Figs. 1(b)–1(f), we illustrate five examples of possible Fe-Ni-B structures found out by our structure searches and structural optimizations. In our Fe-Ni-B structures, Fe and Ni atoms form the basic framework of its tetragonal or orthorhombic structure, whereas B atoms are located at interstitial sites. We discover five additional Fe-Ni-B structures with a tetragonal unit cell, resulting in a total of 10 candidate Fe-Ni-B structures. The optimized lattice constants of 10 candidate Fe-Ni-B structures are given in Table I. The details of the crystallographic data, such as atomic positions, can be available in various file formats at Magnetic Materials Database [51,52].

B. Formation energy

In order to examine the structural stabilities of candidate Fe-Ni-B structures, we calculate the formation energy per

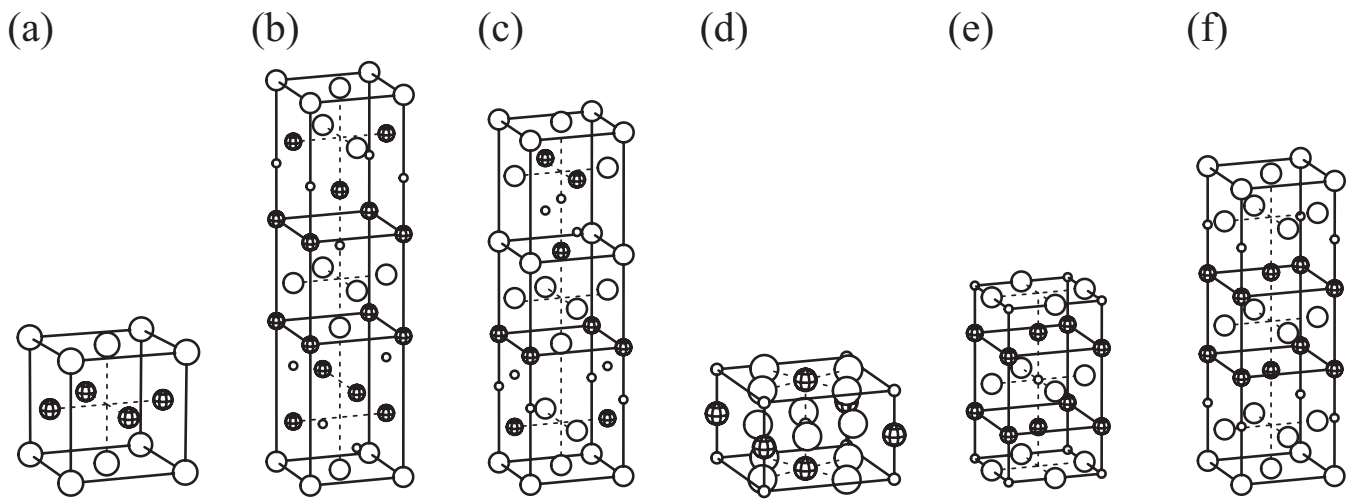

FIG. 1. Crystal structures of Fe-Ni and Fe-Ni-B compounds with a tetragonal or orthorhombic unit cell. Solid and patterned spheres represent Fe and Ni atoms, respectively. Small spheres represent B atoms. (a) $L1_0$-ordered FeNi [$P4/mmm$], (b) $Fe_3Ni_3B_2$ [$Amm2$], (c) Fe_2NiB [$Cmcm$], (d) Fe_4NiB [$I4/m$], (e) Fe_2Ni_2B [$I4/mmm$], and (f) Fe_4Ni_2B [$P4/mmm$].

atom as

$$E_f = \frac{E(\mathrm{Fe}_x\mathrm{Ni}_y B_z) - xE_{\mathrm{Fe}} - yE_{\mathrm{Ni}} - zE_B}{x + y + z}. \quad (3)$$

Here $E(\mathrm{Fe}_x\mathrm{Ni}_y\mathrm{B}_z)$ is the total energy of an $\mathrm{Fe}_x\mathrm{Ni}_y\mathrm{B}_z$ compound. Energy references are the total energies per atom of bulk Fe in the body-centered cubic phase (E_{Fe}), bulk Ni in the face-centered cubic phase (E_{Ni}), and the α-rhombohedral phase of boron (E_B) [56].

Figure 2 shows the compositional phase diagram of an Fe-Ni-B system. In a compositional phase diagram, a set of stable phases forms an energy surface, called the convex hull, which represents theoretical lower boundaries in the formation energy of a system of interest. In Fig. 2, the stable phases in binary subsystems are taken from the Materials Project (MP) database [54,55]. Five metastable Fe-Ni-B structures are registered on the MP database, while no stable ternary phase is reported. Our Fe-Ni-B structures are enriched with

TABLE I. Crystallographic data, formation energy, and calculated magnetic properties of FeNi and B-doped Fe-Ni compounds. Here M_{Fe} (M_{Ni}) is the averaged magnetic moment of Fe (Ni) atom, $\mu_0 M_s$ is the magnetic polarization saturation, K_1 is the magnetocrystalline anisotropy constant, and $\kappa = \sqrt{K_1/(\mu_0 M_s^2)}$ is the magnetic hardness parameter (dimensionless). A complete set of data in this table is available at Magnetic Materials Database [51,52].

	Crystallographic data				Formation energy		Magnetic properties					
	Space group	Lattice constants			E_f	E_{hull}	M_{Fe}	M_{Ni}	$\mu_0 M_s$	K_1		Easy
Material	(No.)	a (Å)	b (Å)	c (Å)	(meV/atom)	(meV/atom)	(μ_B)	(μ_B)	(T)	(MJ/m^3)	κ	axis
	Tetragonal ("$L1_0$-ordered")											
FeNi	$P4/mmm$ (123)	3.56		3.58	−68.9	0	2.66	0.68	1.6	0.3	0.4	c
		3.56[a]		*3.58*[a]			*2.65*[a]	*0.61*[a]		*0.56*[a]		
		3.58[b]		*3.59*[b]					*1.51*[b]	*0.7*[b]	*0.6*	
	Orthorhombic											
$Fe_3Ni_3B_2$	$Amm2$ (38)	3.37	3.39	13.44	18.7	230.6	1.49	0.19	0.8	0.8	1.3	c
Fe_2NiB	$Cmcm$ (63)	3.61	12.93	3.36	124.4	328.0	1.81	0.12	1.1	1.2	1.1	b
	Tetragonal											
Fe_4NiB	$I4/m$ (87)	5.65		3.75	148.6	213.9	1.91	0.39	1.6	1.2	0.8	c
Fe_4Ni_4B	$P4/mmm$ (123)	3.70		6.89	78.8	183.2	2.11	0.73	1.5	1.2	0.9	c
Fe_4Ni_2B	$P4/mmm$ (123)	3.61		11.13	158.4	254.3	1.58	0.57	1.2	1.4	1.1	c
Fe_5NiB	$P4/mmm$ (123)	3.61		11.00	198.9	244.0	1.70	0.45	1.5	0.8	0.7	c
Fe_2Ni_2B	$I4/mmm$ (139)	3.84		6.95	78.0	242.5	1.98	0.54	1.2	1.9	1.3	c
Fe_2Ni_2B	$I4/mmm$ (139)	3.35		17.42	6.2	170.6	1.94	0.41	1.1	1.2	1.1	c
Fe_3NiB	$I4/mmm$ (139)	3.76		14.46	172.4	290.0	1.82	0.67	1.4	−1.4	0.9	ab plane
$Fe_5Ni_3B_2$	$I4/mmm$ (139)	3.36		17.37	44.9	207.6	1.49	0.69	1.0	1.1	1.2	c

[a]Reference [11].
[b]Reference [53].

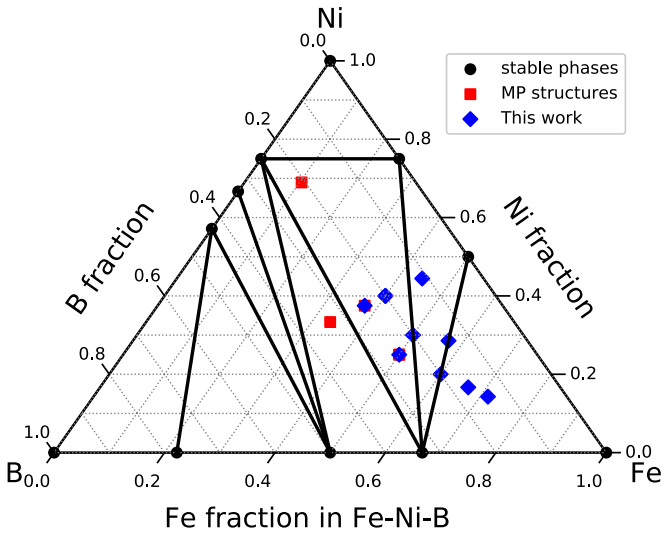

FIG. 2. The compositional phase diagram of an Fe-Ni-B system. The black solid lines indicate a two-dimensional projection of the minimum-energy surface, called the convex hull. The Fe-Ni-B structures from the Materials Project (MP) database [54,55] are also shown for comparison.

Fe, compared to MP structures. From GGA calculations of the formation energy (referenced to elemental phases), E_f, and its value above the convex hull, E_{hull}, we confirm that the candidate Fe-Ni-B structures are metastable. The E_f and E_{hull} values of individual Fe-Ni-B structures are listed in Table I. The calculated formation energies are as low as 0.2–0.3 eV/atom above the convex hull. Synthesis of such metastable Fe-Ni-B structures can be achievable by optimizing experimental conditions. For example, nonequilibrium synthetic method is a promising technique to produce metastable materials, as have been demonstrated for metastable Co_3N phases [18].

C. Magnetic properties

We analyze the density of states (DOS) to understand the impact of B doping on the electronic and magnetic properties of Fe-Ni-B compounds. Here we take a tetragonal Fe_2Ni_2B structure as an example. Figure 3 shows the DOS of Fe_2Ni_2B, compared with that of the $L1_0$-ordered FeNi alloy. The two spectra near the Fermi level are similar. We find a new peak around 6 eV below the Fermi level for Fe_2Ni_2B. The new states are associated with the $2p$ states of boron as shown in Fig. 3. These low-energy states lower the total energy of a system, contributing toward stabilizing a tetragonal Fe-Ni-B structure. The boron $2p$ states hybridize with the $3d$ states from Fe and Ni atoms, resulting in depression of the magnetic moments. The calculated local magnetic moments of Fe and Ni in Fe_2Ni_2B are 1.98 and 0.54 μ_B per atom, respectively. The magnetic moments of other Fe-Ni-B structures are given in Table I.

We list in Table I the calculated magnetic polarization saturation, $\mu_0 M_s$, and magnetic anisotropy constant, K_1, of Fe-Ni-B structures. Table I also includes the magnetic hardness

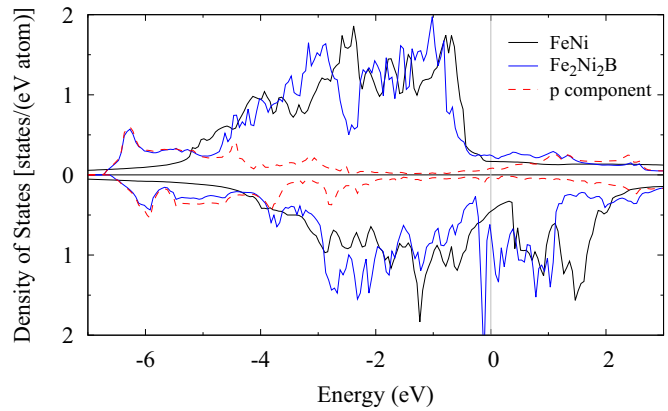

FIG. 3. Comparison of the density of states (DOS) for the majority-spin (upper panel) and minority-spin (lower panel) channels for $L1_0$-ordered FeNi alloy (black) and Fe_2Ni_2B compound (blue). The red dashed spectrum is a projected DOS on p components for Fe_2Ni_2B compound. Energy is referenced to the Fermi level indicated by the gray vertical line.

parameter, defined as

$$\kappa = \sqrt{K_1/(\mu_0 M_s^2)}. \tag{4}$$

This dimensionless parameter measures the strength of the magnetic anisotropy in compared to its magnetic polarization saturation. We find that metastable Fe-Ni-B structures have not only large magnetic anisotropy constants of 1–2 MJ/m^3 but also a high magnetic polarization saturation in excess of 1 T. These numbers are much better than those of the conventional permanent magnets, such as ferrite ($BaFe_{12}O_{19}$). The combination of large values of K_1 and $\mu_0 M_s$ would yield a large maximum energy-product. A tetragonal $I4/mmm$ Fe_2Ni_2B phase with a shorter c-axis

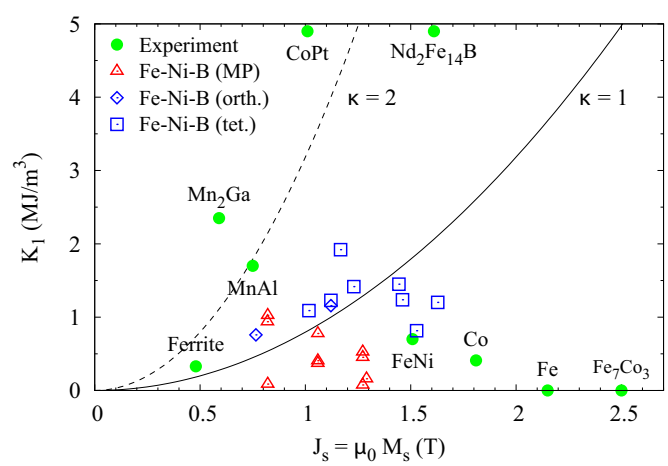

FIG. 4. The magnetocrystalline anisotropy constant, K_1, versus the magnetic polarization saturation, $\mu_0 M_s$, for various magnetic materials including B-doped Fe-Ni compounds with orthorhombic and tetragonal lattices. The parabolic curves indicate the magnetic hardness parameter, κ, of 1 (solid) and 2 (dashed). The results for the Fe-Ni-B structures from the Materials Project (MP) database are shown for comparison.

length is predicted to have the largest K_1 value (1.9 MJ/m^3) among the 10 candidate structures. Due to the enhanced magnetic anisotropy, the magnetic hardness parameter, κ, of the Fe_2Ni_2B phase is estimated to be as large as 1.3. This number is comparable to that of $Nd_2Fe_{14}B$ ($\kappa = 1.54$), one of the widely used rare-earth-based magnets in the current permanent-magnet applications [57]. Our results indicate the great potential of the Fe_2Ni_2B phase as a rare-earth-free permanent-magnet material.

Figure 4 shows a plot of the magnetocrystalline anisotropy constant, K_1, versus the magnetic polarization saturation, $\mu_0 M_s$, for various magnetic materials including B-doped Fe-Ni compounds with orthorhombic and tetragonal lattices. It is evident that our metastable Fe-Ni-B structures are in an advantageous position over ferrite magnets and Mn-based alloys. Most of our Fe-Ni-B structures have better magnetic properties than known metastable Fe-Ni-B structures reported on Materials Project. Five structures of 10 candidate Fe-Ni-B structures are predicted to have not only a large amount of magnetic polarization saturation ($\geqslant$1 T) but also a large magnetic anisotropy constant ($\geqslant$1 MJ/m^3) sufficient for permanent-magnet applications.

V. SUMMARY

We have performed first-principles calculations to explore new rare-earth-free compounds with high magnetocrystalline anisotropy and large magnetic polarization saturation. We have discovered several B-doped Fe-Ni compounds with tetragonal and orthorhombic crystal lattices, and have identified them as metastable phases. We find that these metastable Fe-Ni-B phases can exhibit high magnetocrystalline anisotropy and sufficient magnetic polarization saturation, indicating the potential for replacing rare-earth-based magnets in permanent-magnet applications.

ACKNOWLEDGMENTS

We acknowledge support from a grant from the National Science Foundation (NSF), DMREF-1729202. HPC resources were provided by the Texas Advanced Computing Center (TACC) at The University of Texas at Austin, through the Extreme Science and Engineering Discovery Environment (XSEDE) allocation.

[1] J. M. D. Coey, Scr. Mater. **67**, 524 (2012).
[2] R. Skomski and J. M. D. Coey, Scr. Mater. **112**, 3 (2016).
[3] H. Akai, Scr. Mater. **154**, 300 (2018).
[4] J. M. D. Coey and H. Sun, J. Magn. Magn. Mater. **87**, L251 (1990).
[5] J. F. Herbst, Rev. Mod. Phys. **63**, 819 (1991).
[6] T. Miyake and H. Akai, J. Phys. Soc. Jpn. **87**, 041009 (2018).
[7] G. B. Haxel, J. B. Hedrick, and G. J. Orris, U.S. Geological Survey, Fact Sheet 087-02 (2002).
[8] J. Cui, M. Kramer, L. Zhou, F. Liu, A. Gabay, G. Hadjipanayis, B. Balasubramanian, and D. Sellmyer, Acta Mater. **158**, 118 (2018).
[9] B. Balasubramanian, M. Sakurai, C.-Z. Wang, X. Xu, K.-M. Ho, J. R. Chelikowsky, and D. J. Sellmyer, Mol. Syst. Des. Eng. **5**, 1098 (2020).
[10] L. Néel, J. Pauleve, R. Pauthenet, J. Laugier, and D. Dautreppe, J. Appl. Phys. **35**, 873 (1964).
[11] Y. Miura, S. Ozaki, Y. Kuwahara, M. Tsujikawa, K. Abe, and M. Shirai, J. Phys.: Condens. Matter **25**, 106005 (2013).
[12] L. H. Lewis, A. Mubarok, E. Poirier, N. Bordeaux, P. Manchanda, A. Kashyap, R. Skomski, J. Goldstein, F. E. Pinkerton, R. K. Mishra, R. C. K. Jr., and K. Barmak, J. Phys.: Condens. Matter **26**, 064213 (2014).
[13] K. Takanashi, M. Mizuguchi, T. Kojima, and T. Tashiro, J. Phys. D: Appl. Phys. **50**, 483002 (2017).
[14] T. Burkert, L. Nordström, O. Eriksson, and O. Heinonen, Phys. Rev. Lett. **93**, 027203 (2004).
[15] B. Balasubramanian, B. Das, M. C. Nguyen, X. Xu, J. Zhang, X. Zhang, Y. Liu, A. Huq, S. R. Valloppilly, Y. Jin, C.-Z. Wang, K.-M. Ho, and D. J. Sellmyer, APL Mater. **4**, 116109 (2016).
[16] X. Xu, X. Zhang, Y. Yin, B. Balasubramanian, B. Das, Y. Liu, A. Huq, and D. J. Sellmyer, J. Phys. D: Appl. Phys. **50**, 025002 (2016).
[17] T. Miyake, K. Terakura, Y. Harashima, H. Kino, and S. Ishibashi, J. Phys. Soc. Jpn. **83**, 043702 (2014).
[18] B. Balasubramanian, X. Zhao, S. R. Valloppilly, S. Beniwal, R. Skomski, A. Sarella, Y. Jin, X. Li, X. Xu, H. Cao, H. Wang, A. Enders, C.-Z. Wang, K.-M. Ho, and D. J. Sellmyer, Nanoscale **10**, 13011 (2018).
[19] M. Sakurai, X. Zhao, C.-Z. Wang, K.-M. Ho, and J. R. Chelikowsky, Phys. Rev. Mater. **2**, 024401 (2018).
[20] X.-Z. Li, W.-Y. Zhang, S. Valloppilly, and D. J. Sellmyer, Sci. Rep. **9**, 7762 (2019).
[21] H. Wang, B. Balasubramanian, R. Pahari, R. Skomski, Y. Liu, A. Huq, D. J. Sellmyer, and X. Xu, Phys. Rev. Mater. **3**, 064403 (2019).
[22] P. Hohenberg and W. Kohn, Phys. Rev. **136**, B864 (1964).
[23] W. Kohn and L. J. Sham, Phys. Rev. **140**, A1133 (1965).
[24] M. C. Payne, M. P. Teter, D. C. Allan, T. A. Arias, and J. D. Joannopoulos, Rev. Mod. Phys. **64**, 1045 (1992).
[25] R. M. Martin, *Electronic Structure: Basic Theory and Practical Methods* (Cambridge University Press, Cambridge, 2004).
[26] J. R. Chelikowsky, N. Troullier, and Y. Saad, Phys. Rev. Lett. **72**, 1240 (1994).
[27] J. R. Chelikowsky, N. Troullier, K. Wu, and Y. Saad, Phys. Rev. B **50**, 11355 (1994).
[28] L. Kronik, A. Makmal, M. L. Tiago, M. M. G. Alemany, M. Jain, X. Huang, Y. Saad, and J. R. Chelikowsky, Phys. Status Solidi B **243**, 1063 (2006).
[29] M. L. Tiago, Y. Zhou, M. M. G. Alemany, Y. Saad, and J. R. Chelikowsky, Phys. Rev. Lett. **97**, 147201 (2006).
[30] D. Naveh and L. Kronik, Solid State Commun. **149**, 177 (2009).
[31] J. Souto-Casares, M. Sakurai, and J. R. Chelikowsky, Phys. Rev. B **93**, 174418 (2016).
[32] M. Sakurai, J. Souto-Casares, and J. R. Chelikowsky, Phys. Rev. B **94**, 024437 (2016).
[33] M. Sakurai and J. R. Chelikowsky, Phys. Rev. Mater. **3**, 044402 (2019).
[34] A. K. Rajagopal and J. Callaway, Phys. Rev. B **7**, 1912 (1973).

[35] A. H. MacDonald and S. H. Vosko, J. Phys. C **12**, 2977 (1979).
[36] J. P. Perdew, K. Burke, and M. Ernzerhof, Phys. Rev. Lett. **77**, 3865 (1996).
[37] P. E. Blöchl, Phys. Rev. B **50**, 17953 (1994).
[38] G. Kresse and D. Joubert, Phys. Rev. B **59**, 1758 (1999).
[39] A. Dal Corso, Phys. Rev. B **82**, 075116 (2010).
[40] M. Sakurai and J. R. Chelikowsky, Phys. Rev. Mater. **2**, 084411 (2018).
[41] P. Giannozzi *et al.*, J. Phys.: Condens. Matter **21**, 395502 (2009).
[42] P. Giannozzi *et al.*, J. Phys.: Condens. Matter **29**, 465901 (2017).
[43] S. G. Louie, S. Froyen, and M. L. Cohen, Phys. Rev. B **26**, 1738 (1982).
[44] H. J. Monkhorst and J. D. Pack, Phys. Rev. B **13**, 5188 (1976).
[45] Y. Zhou, Y. Saad, M. L. Tiago, and J. R. Chelikowsky, Phys. Rev. E **74**, 066704 (2006).
[46] Y. Zhou, Y. Saad, M. L. Tiago, and J. R. Chelikowsky, J. Comput. Phys. **219**, 172 (2006).
[47] Y. Zhou, J. R. Chelikowsky, and Y. Saad, J. Comput. Phys. **274**, 770 (2014).
[48] J. Winterlik, B. Balke, G. H. Fecher, C. Felser, M. C. M. Alves, F. Bernardi, and J. Morais, Phys. Rev. B **77**, 054406 (2008).
[49] X. Zhao, L. Ke, C.-Z. Wang, and K.-M. Ho, Phys. Chem. Chem. Phys. **18**, 31680 (2016).
[50] X. Zhao, C.-Z. Wang, Y. Yao, and K.-M. Ho, Phys. Rev. B **94**, 224424 (2016).
[51] M. Sakurai, R. Wang, T. Liao, C. Zhang, H. Sun, Y. Sun, H. Wang, S. Wang, B. Balasubramanian, X. Xu, D. J. Sellmyer, C.-Z. Wang, K.-M. Ho, and J. R. Chelikowsky (unpublished).
[52] Visit https://magmatdb.herokuapp.com/ for Magnetic Materials Database.
[53] T. Kojima, M. Ogiwara, M. Mizuguchi, M. Kotsugi, T. Koganezawa, T. Ohtsuki, T.-Y. Tashiro, and K. Takanashi, J. Phys.: Condens. Matter **26**, 064207 (2014).
[54] A. Jain, S. P. Ong, G. Hautier, W. Chen, W. D. Richards, S. Dacek, S. Cholia, D. Gunter, D. Skinner, G. Ceder, and K. A. Persson, APL Mater. **1**, 011002 (2013).
[55] https://materialsproject.org.
[56] B. F. Decker and J. S. Kasper, Acta Crystallogr. **12**, 503 (1959).
[57] O. Gutfleisch, M. A. Willard, E. Brück, C. H. Chen, S. G. Sankar, and J. P. Liu, Adv. Mater. **23**, 821 (2011).